Taylor & Francis
Taylor & Francis Group

Large-scale fluctuations and dynamics of the Bullard–von Kármán dynamo

GAUTIER VERHILLE, NICOLAS PLIHON*, GRÉGORY FANJAT,
ROMAIN VOLK, MICKAEL BOURGOIN and JEAN-FRANÇOIS PINTON

Laboratoire de Physique de l'École Normale Supérieure de Lyon,
CNRS & Université de Lyon, F-69364, Lyon, France

A synthetic fluid dynamo built in the spirit of the Bullard device (Bullard, The stability of a homopolar dynamo, *Proc. Camb. Phil. Soc.* 1955, **51**, 744) is investigated. It is a two-step dynamo in which one process stems from the fluid turbulence, while the other part is achieved by a linear amplification of currents in external coils (Bourgoin *et al*., A bullard-von Kármán dynamo, *New J. Phys.*, 2006, **8**, 329). Modifications in the forcing are introduced in order to change the dynamics of the flow, and hence the dynamo behavior. Some features, such as on–off intermittency at onset of dynamo action, are very robust. Large-scale fluctuations have a significant impact on the resulting dynamo, in particular in the observation of magnetic field reversals.

Keywords: Magnetohydrodynamics; Dynamo; Bifurcation; Turbulence; On–off intermittency

1. Introduction

$\alpha - \omega$ dynamo models are extensively used in the description of natural dynamos (Brandenburg and Subramanian 2005). In these approaches, the ω-effect converts a poloidal field into a toroidal component, while the α-effect is invoked for the conversion back from toroidal to poloidal. In planets, the electrically conducting fluid is a molten metal (iron for the Earth), i.e., a fluid with a very low-magnetic Prandtl number. As a consequence, turbulence has to be fully developed for induction effects to be able to overcome (Joule) dissipation, and hence induce a dynamo. Turbulent dynamos have been extensively studied in the context of mean-field hydrodynamics (Moffatt 1978, Krause and Rädler 1980). In this approach, the turbulent small-scale induction processes contribute to the dynamics of the large-scale magnetic field through the mean electromotive force $\overline{\epsilon}_i = \alpha_{ij}\overline{B_j} + \beta_{ijk}\partial_j\overline{B_k}$ (the reader is referred to Rädler and Stepanov (2006) for generalized expressions). The α and β tensors depend on the small-scale turbulence, and expressions for them have been established in several contexts.

---

*Corresponding author. Email: nicolas.plihon@ens-lyon.fr

Measurements, however, have revealed that their contribution is small, at least at low-magnetic Prandtl numbers and moderate magnetic Reynolds numbers (Stepanov *et al.* 2006, Denisov *et al.* 2008, Noskov *et al.* 2009). An α contribution can also originate from large-scale motions through Parker's stretch and twist mechanism (Pétrélis *et al.* 2003, Bourgoin *et al.* 2004a). Recently, the observation of a self-sustained axisymmetric magnetic field in the VKS experiment (von Kármán Sodium experiment) (Monchaux *et al.* 2007) has been modeled as an $\alpha - \omega$ dynamo (Pétrélis *et al.* 2007, Aumaître *et al.* 2008, 2009, Laguerre *et al.* 2008). This experiment has also revealed a rich time-dynamics of the magnetic field (Berhanu *et al.* 2007, Monchaux *et al.* 2008, Berhanu *et al.* 2009), raising issues concerning the contribution of flow fluctuations on the dynamo behavior. It has been shown, indeed, in several studies that von Kármán flows display large fluctuations at very low frequency in time (Ravelet *et al.* 2004, 2008, de la Torre and Burguete *et al.* 2007) which have a leading role on magnetic induction characteristics (Volk *et al.* 2006).

In the present study we consider experimental synthetic dynamos (Bourgoin *et al.* 2006) based on the device originally proposed by Bullard (1955), in which an α-effect is modeled by means of an external wiring, while a second induction process originates from the flow itself and takes into account the full turbulent fluctuations. This turbulent induction effect is linked to the flow differential rotation and has been extensively studied in previous experimental (Odier *et al.* 1998, Volk *et al.* 2006) and numerical works (Bourgoin *et al.* 2004b): for instance, if a magnetic field is applied parallel to the cylinder axis by a set of coils, the fluid differential rotation induces a toroidal magnetic field (the so-called ω-effect). Since the flow is fully turbulent (with integral kinetic Reynolds exceeding 10^5), the induced toroidal magnetic field is highly fluctuating: this ω-effect fully incorporates the flow turbulence. An effective α-effect is then achieved when the intensity of the induced toroidal field is used to control a linear amplifier driving the current in the coils. This amplification effect actually replaces a fluid α-effect usually invoked in dynamo theory. In order to avoid confusion, this effective α-effect (which is a synthetic poloidal to toroidal conversion process) will be termed A-effect for amplification-effect. Such a feedback loop thus generates a dynamo (for instance, an $A - \omega$ dynamo for the case described above).

The main goal of the present study is to characterize how the resulting dynamo bifurcation and magnetic field dynamics are affected when large-scale properties of the von Kármán flow are modified by the insertion of various appendices inside the vessel (Ravelet 2005, Cortet *et al.* 2009), or when rotating the impellers at unequal rates – as a way to impose global rotation onto the flow (Ravelet *et al.* 2004).

The experimental setup is described in detail in section 2. The dynamics of the synthetic Bullard–von Kármán dynamos are described and analyzed in section 3. Conclusions are drawn in section 4.

2. Experimental setup

2.1. *von Kármán gallium flow*

The synthetic Bullard–von Kármán dynamo is built upon a von Kármán flow. This flow is produced by the rotation of two impellers inside a stainless steel cylindrical vessel filled with liquid gallium. The cylinder radius R is 97 mm and its length is

323 mm. The impellers have a radius equal to 82.5 mm and are fitted to a set of eight blades with height 10 mm. They are separated by a distance $H = 203$ mm. The impellers are driven by two AC-motors which provide a constant rotation rate in the interval $(F_1, F_2) \in [0.5, 25]$ Hz. In most of the cases, the flow is driven by symmetric forcing at $F_1 = F_2 = F$. The system is cooled by a water circulation located behind the driving impellers; the experiments are run at a temperature between 40°C and 48°C. Liquid gallium has density $\rho = 6.09 \times 10^3 \, \text{kg m}^{-3}$, electrical conductivity $\sigma = 3.68 \times 10^6 \, \text{Ohm}^{-1} \, \text{m}^{-1}$, hence a magnetic diffusivity $\lambda = (\mu_0 \sigma)^{-1} = 0.29 \, \text{m}^2 \, \text{s}^{-1}$. Its kinematic viscosity is $\nu = 3.1 \times 10^{-7} \, \text{m}^2 \, \text{s}^{-1}$. The integral kinematic and magnetic Reynolds numbers are defined as $\text{Re} = 2\pi R^2 F / \nu$ and $R_m = 2\pi R^2 F / \lambda$. Values of R_m up to 5 are achieved, with corresponding Re in excess of 10^6. The time-average structure of the flow driven by impellers at exact counter-rotation consist of two cells rotating with opposite toroidal velocities and two recirculation loops close to the impellers, separated by a large shear-layer in the mid plane (see figure 8(b) top in section 3.3.1 for a sketch).

Magnetic induction measurements are performed using Hall sensor probes inserted into the flow in the mid plane. Data are recorded using a National Instrument PXI-4472 digitizer at a rate of 1000 Hz with a 23 bits resolution.

2.2. *Dynamo loops*

2.2.1. Axial dipole.
A first dynamo configuration which generates an axial dipole is shown in figure 1(a). As the flow is forced by counter-rotating impellers, the differential rotation in the fluid motion induces an azimuthal magnetic field B_θ^I when an applied axial magnetic field B_z^A is imposed by axial coils; this is the ω-effect (Moffatt 1978). This induced azimuthal field is measured from a local probe in the mid plane at $r = 0.56R$; the position of the probe was chosen such as to maximize the measured azimuthal field (Volk *et al.* 2006). The measured value is then amplified to drive the current source which feeds currents into the axial coils. This external amplification replaces an α part of the dynamo cycle, since an axial field stems from an azimuthal one. The feedback amplification is linear ($I_{\text{coils}} \propto B_\theta^I$ up to a saturation value $I_{\text{coils}}^{\text{sat}}$, which is the maximum current that can be drawn from the current source). The main component of the resulting dynamo is an axial dipole.

For all available values of the rotation rate of the driving impellers, the magnetic Reynolds number is low enough to be in a quasi-static approximation. In this regime, $B_\theta^I \sim (\Delta^{-1}/\lambda) B_z^A \partial_z v_\theta$, where v_θ is the azimuthal velocity (Bourgoin *et al.* 2004a). The ω part of the dynamo cycle is thus very much dependent on the statistical properties of the velocity gradients at all scales.

2.2.2. Equatorial dipole.
Another possibility is to arrange the external coils so that they generate a field perpendicular to the rotation axis, say B_x (an equatorial dipole). In this case, the induced magnetic field component which drives the current source is the axial induction $B_z^{\pi/2}$ measured in the mid-plane at 90° from the applied field.

This induction effect is linear in R_m and is mainly due to a boundary-condition effect linked to the jump in electrical conductivity at the wall. This process is described in detail in Bourgoin *et al.* (2004b) and only briefly discussed here. The flow rotation on the imposed field B_x induces a B_y component in opposite direction in each flow cell.
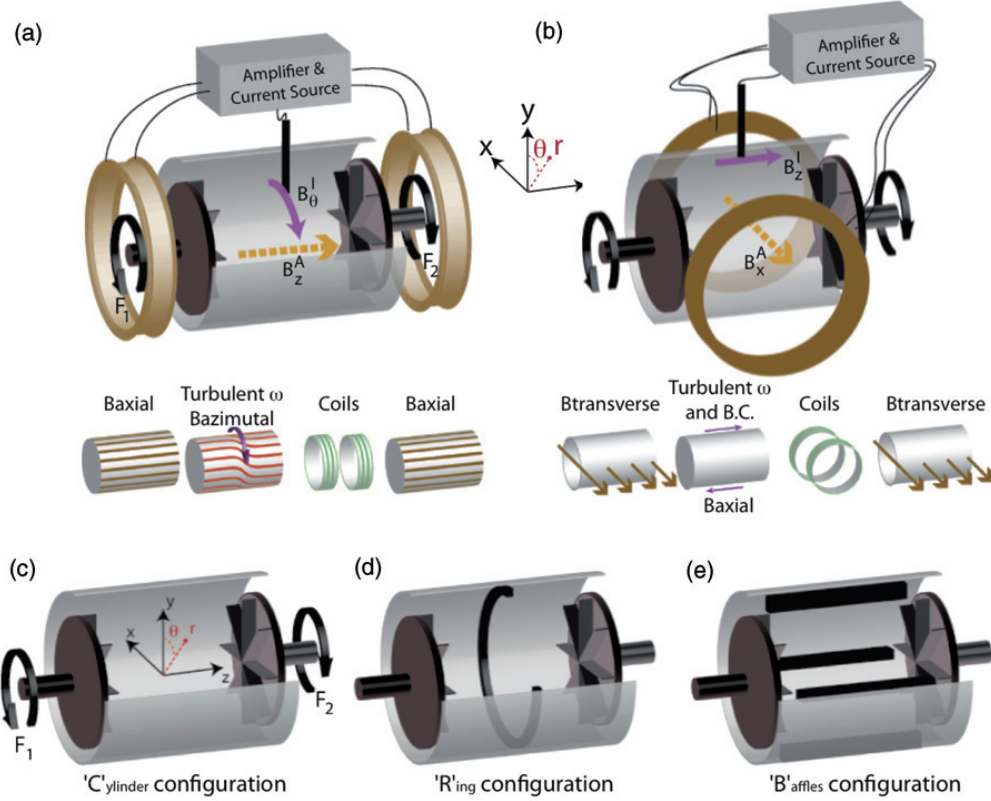
Figure 1. Experimental setup: a von Kármán flow of liquid gallium is generated in a cylindrical vessel between two counter rotating impellers driven by two AC-motors. (a) Synthetic $A - \omega$ dynamo (axial dipole), the turbulent-induced azimuthal field is measured at $0.56R$ in the mid-plane between impellers. (b) Synthetic $A - BC$ dynamo (equatorial dipole), the turbulent-induced axial field is measured at $0.87R$ in the mid-plane between impellers. (c) Cylinder (C) configuration of the vessel and coordinate axis. (d) Ring (R) configuration and (e) Baffles (B) configuration.

This induced field is associated with a current field in the direction of the applied field in both cells, and opposite in the shear layer. As the outside medium is electrically insulating, these currents have to loop back in the flow volume and thus induce an axial component at the flow boundary that diffuses inside the flow. Numerical studies have shown that, in the quasi-static approximation, the current density source term is linked to the deformation of the transverse magnetic field by the flow $\Delta \mathbf{j} = \mu_0^{-1}(\mathbf{B} \cdot \nabla)\boldsymbol{\omega}$, where $\boldsymbol{\omega}$ is the flow vorticity. The jump in electrical conductivity $[\lambda]_S$ at the wall S then induces a magnetic field $\Delta \mathbf{B} = [\lambda]_S \delta_S \mu_0 \mathbf{j} \times \mathbf{n}$, where $\mathbf{n}$ is the outgoing direction and δ_S a Dirac distribution non-null on S. The induced field is axial and maximum near the vessel wall and proportional to the radial vorticity in the shear-layer since the structures of $\mathbf{j}$ and $\Delta \mathbf{j}$ are similar.

In the following we will refer to this mechanism as *BC*-effect, for *boundary-conditions effect*. The induced axial field is measured from a local probe in the mid-plane at $r = 0.87R$ and its value is then amplified to drive the current source which feeds currents into the transverse coils. The equatorial dipole dynamo is of $A - BC$ type.

In von Kármán flows, the *BC*-effect is particularly intense because large-scale radial vortices develop in the mid-plane as a result of a Kelvin–Helmholtz-like instability in the shear layer (de la Torre and Burguete *et al.* 2007, Ravelet *et al.* 2008). These radial vortices are, moreover, known to have a highly fluctuating dynamics which in turn generates strong fluctuations of the *BC*-induced field.

2.2.3. Implementation. Effective magnetic Reynolds numbers defined from the turbulent induction processes (as a ratio of induced field to applied field) are in the range $[3 \times 10^{-3} F_i; 2 \times 10^{-2} F_i]$ and well below the required values for dynamo threshold (32 for the VKS experiment (Monchaux *et al.* 2007)). This limitation is bypassed in our Bullard–von Kármán setup by using a linear amplifier of gain G. For each configuration G is kept constant – the control parameter thus being the rotation frequency of the impellers F_i – but G is adjusted from one configuration to the other by the following procedure.

One first proceeds to induction measurements (or "open-loop" measurements): a large-scale, time-independent magnetic field, B^A is applied by the external coils. A turbulent-induced magnetic field B^I is generated by the turbulent flow. From measurements of the induced field, a effective conversion factor A_{eff} of the induction process is defined as $\langle B^I \rangle_t = A_{\text{eff}} F \langle B^A \rangle_t$, where $\langle . \rangle_t$ is the time-averaging operator.

The amplifier provides the other conversion process of the dynamo, $B^A = GB^I$. One sets the gain G of amplifier such that a dynamo threshold estimated from time-averaged measurements $F_c = (GA_{\text{eff}})^{-1}$ is constant and equal to 8.3 Hz for all configurations. In other words, the gain is adjusted such that, for a given flow forcing parameter F, the time-averaged value of the amplified-induced field $G\langle B^I \rangle_t$ is constant whatever the flow configuration and dynamo type. We emphasize here that the actual feedback process does not involve any averaging procedure and that the actual threshold may be shifted from 8.3 Hz by the turbulent fluctuations as was already observed in other physical situations (Berthet *et al.* 2003).

Saturation is set by the maximum current available from the source; the saturated magnetic field value is of the order of a few tens of Gauss. As a result, the Lorentz force is too weak to react back onto the flow field (the interaction parameter is less than 10^{-2}). The synthetic Bullard–von Kármán is thus similar to a kinematic dynamo.

2.3. *Flow configurations*

The scope of the present study is to investigate the influence of the flow dynamics on the behavior of the self-sustained magnetic field. Modifications are achieved by changing the flow, either by inserting appendices to the inner wall of the cylinder or by driving the flow asymmetrically (i.e., rotating the impellers at different speeds).

Three geometric configurations have been tested. They are shown in figures 1((c)–(e)). In the base configuration (hereafter called C for Cylinder) there is no attachment. In configuration B, four longitudinal baffles are attached; they are rectangular pieces 150 mm long, 10 mm tall, and 10 mm thick, mounted parallel to the cylinder axis. In configuration R, a ring is attached in the mid-plane; it is 15 mm tall and 4 mm thick. The respective influence of these attachments have been studied in water experiments (Ravelet 2005, Cortet *et al.* 2009), where it was found that they modify significantly the dynamics of the differential shear layer in the mid-plane (although these studies were achieved with curved blades, these observations should remain similar at leading order in our device). The presence of ring or baffles tends to stabilize the central shear layer. Appendices also modify the number and time evolution of the radial vortices in the shear layer. In the C configuration, three large radial vortices fluctuating in size and position are present. In the B configuration, four vortices are positioned in-between baffles. In the R configuration, the three vortices are splitting in pairs; in our

configuration their mobility and fluctuations remain unresolved (see Cortet *et al.* (2009) for a detailed analysis).

Similarly, when the flow is driven by counter-rotating the impellers at different speeds, the flow bifurcates between 2-cell and 1-cell configurations (Ravelet *et al.* 2004, de la Torre and Burguete *et al.* 2007, Cortet *et al.* 2009), hence leading to substantial modifications of the flow turbulence and large-scale topology. The unbalance in the driving of the flow is measured by the ratio $\Theta = (F_1 - F_2)/(F_1 + F_2)$; $\Theta = 0$ corresponding to exact counter-rotation and $\Theta = 1$ to the fluid being set into motion by the rotation of one impeller only. The transition occurs at a critical value of Θ above which the shear layer abruptly moves from the mid-plane to the vicinity of the slower impeller (the flow transits then from a two counter-rotating cells geometry to a single cell geometry). It is associated with an abrupt change in the mechanical power required to keep the impellers rotating at fixed rates, and a sharp increase in the kinetic energy fluctuations.

Altogether, by inserting appendices in the flow or driving it asymmetrically, one has the possibility to vary the mean profiles and fluctuation characteristics of the von Kármán flow. The impact of these changes on the synthetic $A - \omega$ and $A - BC$ dynamos is studied in detail below. Note that though both ω and BC effects are primarily generated by the same differential rotation, they are sensitive to different topological properties, also with different dynamical behavior of the mid-plane shear layer: the BC-effect is sensitive to the radial vorticity (ω_r) in the vicinity of the vessel wall, while the ω-effect is sensitive to the axial change of the toroidal velocity in the bulk of the flow. The natural fluctuations of these flow gradients are known to be of different kinds: radial vorticity fluctuations are closely linked to the dynamic of strong intermittent Kelvin–Helmhotz vortices in the shear layer, while the axial gradient of toroidal velocity fluctuates according to local and global displacements of the shear layer. Exploring both the axial and equatorial dipoles' configurations then give us a way to probe selectively the impact of these velocity gradients on the dynamo.

3. Dynamo and flow dynamics

3.1. *Axial dipole, $A - \omega$ dynamo*

In this section, the flow is driven symmetrically: impellers counter rotate at the same rate $F = F_1 = F_2$. The external coils are set to generate an axial dipole field. The turbulent ω-effect (the source of the fluctuations for the dynamo) is first analyzed as an induction process on its own. Dynamical features of the $A - \omega$ dynamos are then described and analyzed.

3.1.1. Turbulent ω induction. We first consider induction measurements obtained when a constant axial magnetic field is applied. We show the temporal dynamics of the induced field in figure 2(b), and display the probability density functions (PDFs) and time spectra of $B_\theta/\langle B_\theta \rangle$ in figures 2(c) and (d). Note that in order to compare the fluctuations for the different configurations, we have normalized the induced field by its mean amplitude in figures 2(c) and (d). Indeed, in the dynamo loop, the value of the
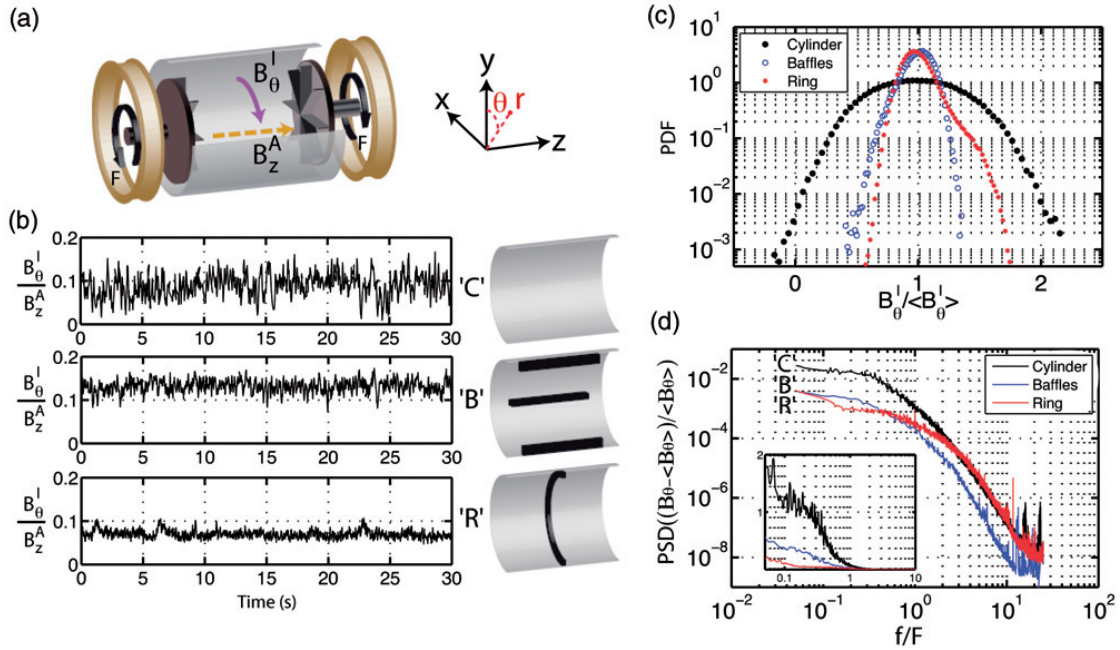
Figure 2. Axial applied field, azimuthal induction features at $r = 0.56R$. (a) Experimental setup and (b) temporal dynamics for the three flow configurations. (c) Probability density functions and (d) power spectrum density of the azimuthal induced field (log–lin representation in the inset). Note that, for the last two graphs, the induced fields are normalized by their time-averaged values.

gain G is adjusted so that the amplified time-averaged induced field for a fixed rotation rate is the same whatever the flow configuration.

- *C* configuration. The shear layer is fully developed in this less constrained state. As a result, its motion explores a large portion of the flow volume. These motions result in large variations of the amplitude of the induced field, with a quasi-Gaussian statistics. The power spectrum of fluctuations in time reveals an important low frequencies dynamics. These features have been discussed in detail in previous studies (Volk *et al.* 2006).
- *R* configuration. When a ring is installed in the mid-plane, the shear layer is pinned (Ravelet 2005, Cortet *et al.* 2009). The axial gradient of the time-averaged azimuthal velocity is peaked at the ring position (Ravelet 2005) and higher than in the *C* configuration. The time-averaged azimuthal-induced field is nevertheless of the same order of magnitude in both configurations (cf. figure 2(b)). This is because the magnetic field "filters" the velocity gradients at a length scale of the order of the magnetic diffusion length $\eta_B \sim \sqrt{\lambda/F} \sim 5\,\mathrm{cm}$ at $R_m = 2$. The magnetic field is more sensitive to the difference of velocity on either side of the shear layer rather than in the actual slope of the velocity profile.

  Another effect is that fluctuations in the azimuthal induction are reduced due to the shear pinning. The time spectra for the two configurations are similar in the inertial range, but the presence of the ring reduces low-frequency fluctuations. The ring acts as high-pass filter for velocity fluctuations and associated radial vortices emerging from the shear layer dynamics (Cortet *et al.* 2009). The slight peak at very low frequency is attributed to a "depinning"
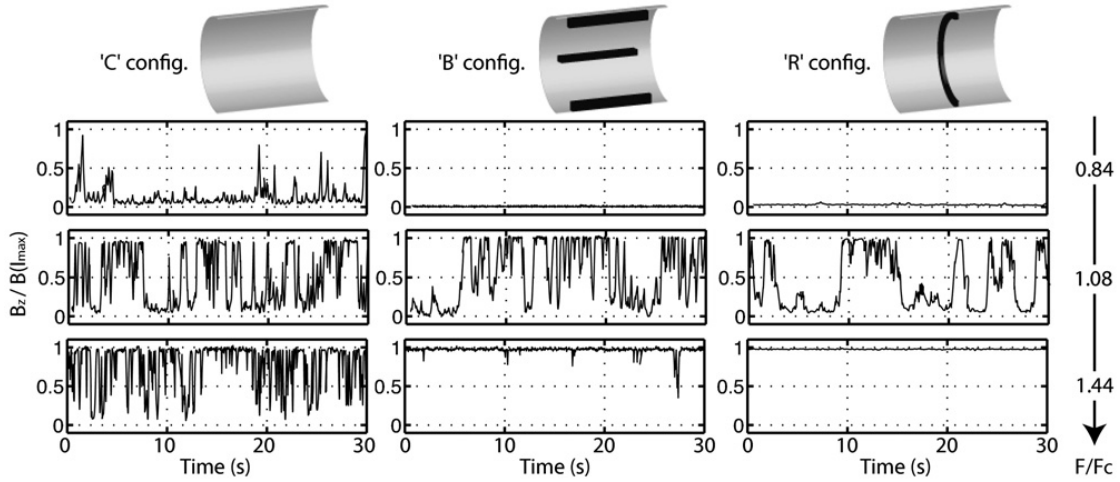
Figure 3.   Axial dipole dynamo temporal features: temporal evolution of the dipole amplitude as a function of driving frequency for the three configurations.

occurring at irregular time intervals, also observed as a bimodality in the PDF in figure 2(c).

- *B* configuration. When baffles are inserted in the vessel, vortices of the shear layer are confined to inter-baffles position and fluctuations of the shear layer are also damped (Ravelet 2005). Like in the *R* configuration, the time-averaged induced field is weakly modified, but fluctuations are highly reduced as compared to the *C* configuration.

For these three configurations, the mean-induced field and normalized fluctuations for $R_m = 2$ are the following: $\langle B_\theta^I / B_z^A \rangle = 0.08; 0.12; 0.07$ and $(B_\theta^I)_{\text{rms}} / \langle B_\theta^I \rangle = 0.32; 0.11; 0.1$ for the *C*, *B* and *R* configurations, respectively. Comparison of the spectra (figure 2(d)) show that modifications of the flow strongly modify the low-frequency, large-scale dynamics of the turbulent induction, while keeping small-scale (inertial range) dynamics almost unchanged.

3.1.2. Dynamo: axial dipole.   We then analyze the behavior of the synthetic $A - \omega$ dynamo (i.e., when the measured azimuthal field actually drives the current in the induction coils). Time signals of the axial magnetic field (normalized to the maximum field) are shown in figure 3 for the three configurations and an increasing forcing parameter F (from top to bottom). For the three configurations and whatever the value of the forcing parameter, the axial dipole dynamo is always observed homopolar: when growing in either polarity, the field remained of same polarity. However, both polarities were observed for different realizations (i.e., when stopping the motors and increasing the rotation rate above the critical value), as is expected from the $\mathbf{B} \rightarrow -\mathbf{B}$ symmetry of the MHD equations.

Let us first analyze the *C* configuration, for which last section showed that fluctuations of the ω-effect are the highest. At very low rotation rates $F \ll F_c$, the magnetic field is null. When the rotation rate increases and approaches the threshold ($F \lesssim F_c$), the magnetic field remains null most of the time, but exhibits intermittent bursts. The density and duration of the dynamo state increase rapidly with the impellers rotation rate: as $F > 1.3 F_c$, the magnetic field in mostly non-zero, with intermittent
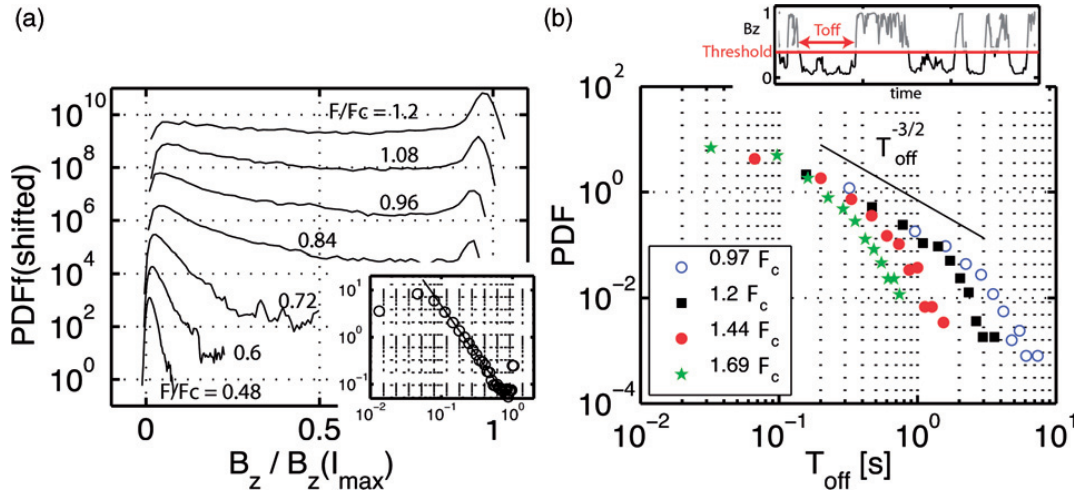
Figure 4. Axial dipole dynamo for the *C* configuration: (a) evolution of the PDF of the axial magnetic field as a function of the driving parameter – inset: log–log plot for $F = 0.84F_c$- and (b) – inset: definition of inter-burst time interval – main: evolution of the PDF of the inter-burst intervals as a function of the driving parameter.

extinctions for short time intervals. The system thus bifurcates from a non dynamo to a dynamo state via an on–off intermittency scenario, also previously observed in numerical models of the dynamo (Sweet *et al*. 2001, Alexakis and Ponty *et al*. 2008). This kind of bifurcation is characterized by specific features of the signal: its PDF is peaked at zero near onset and then decays algebraically; the PDFs of "off" times scales as $T_{\text{off}}^{-3/2}$ (Heagy *et al*. 1994).

Evolution of the measured PDFs of magnetic field as a function of the forcing parameter is shown in figure 4(a). The PDF is peaked at zero for rotation frequencies up to $1.2F_c$, and extends to large values, even at low-rotation frequencies. A log–log representation is shown in inset of figure 4(a) and shows a typical negative power-law for the PDF (with an exponent proportional to the control parameter). This feature was observed in numerical simulation of on–off models (Aumaître *et al*. 2005, 2006) and simulations of MHD equations (Sweet *et al*. 2001). On–off intermittent signals also display an universal behavior of inter-burst time intervals, or time interval between dynamo activity, named T_{off} –for "off" phases or laminar phases. This time interval is defined in the inset of figure 4(b): one sets a threshold and computes the time T_{off} for which the dynamo field is below this threshold. The PDFs of T_{off} are displayed in figure 4(b) for four values of the forcing parameter. These PDFs have a power-law dependence with a cut-off at large values (the distribution of the "off" phases has been checked to be independent of the value of the threshold). A $T_{\text{off}}^{-3/2}$ scaling is shown for comparison with the experimental data, showing that the data statistics is in agreement with the $-3/2$ power-law scaling behavior predicted for on–off intermittency (Heagy *et al*. 1994), observed in numerical simulations (Sweet *et al*. 2001, Aumaître *et al*. 2005, 2006) or in experimental investigations in electronic circuits (Hammer *et al*. 1994), gas-discharge plasmas (Feng *et al*. 1998), or convection in liquid crystals (John *et al*. 1999). Corrections to the power-law scaling are not obvious, so that more complex scenarii (such as "in–out" intermittency (Covas *et al*. 2001)) may not apply here.

The variation of the cut-off time in the PDF of T_{off} with the control parameter is steep. We observe a power-law with a -5 exponent in a small range $F \in [0.97F_c, 1.69F_c]$.
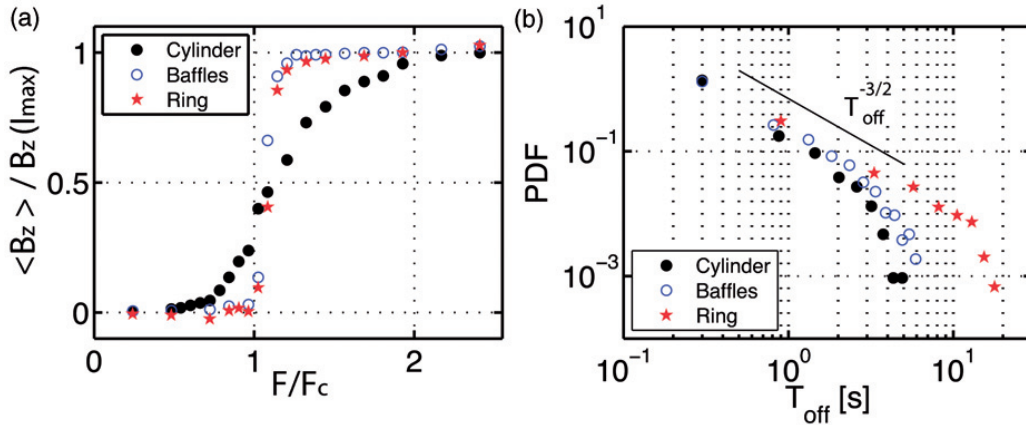
Figure 5. Features of the axial dipole dynamo: (a) evolution of the time-averaged axial magnetic field as a function of the rotation frequency for the three configurations; (b) PDF of the inter-burst time interval for the three configurations at $F = 1.08 F_c$.

This is in contrast with numerical models with multiplicative noise for which a decay as F^{-2} is quoted (Aumaître *et al.* 2006).

Modifications of the ω-effect with the other two configurations drastically change the dynamo features. As can be seen in figure 3, for the B and R configurations, no dynamo bursts are observed for impellers rotation rates well below threshold and "off" phases are no longer present well above the threshold. The associated bifurcation curves are displayed in figure 5(a). The bifurcation is steeper for the B and R configurations as compared to the C configuration, i.e., the width of the intermittent domain decreases when inserting appendices in the vessel. The on–off intermittent regime is nevertheless always observed in a very narrow range near onset. Figure 5(b) shows the PDFs of the "off" phases for the three configurations near the critical rotation rate ($F = 1.08 F_c$). The $-3/2$ power-law scaling is independent of the configuration, while the exponential cut off increases when the low-frequency component of fluctuations decreases. The mean length of "on" phases also significantly increases when low frequencies of the noise decrease, as can be observed in figure 3.

As a partial conclusion, we observe that several features (such as the on–off scenario and waiting times statistics) of the axial dynamo at onset are robust with respect to large-scale modifications of the von Kármán flow. Other features (such as the width of the transition and the frequency of incursions to or from dynamo states) are on the contrary strongly dependent on the large-scale dynamics of the flow.

3.2. *Equatorial dipole, A − BC dynamo*

We now consider the $A - BC$ dynamo configuration, generating an equatorial dipole field, perpendicular to the axis of rotation of the impellers. As for the axial case, we study the dynamo bifurcation in the C, B and R configurations, the flow being driven symmetrically with the impellers counter rotating at the same rate $F = F_1 = F_2$. As for the previous section, the gain of the feedback loop is adjusted for each configuration in order to keep constant the dynamo threshold estimated from time-averaged induction measurements ($F_c = 8.3$ Hz).
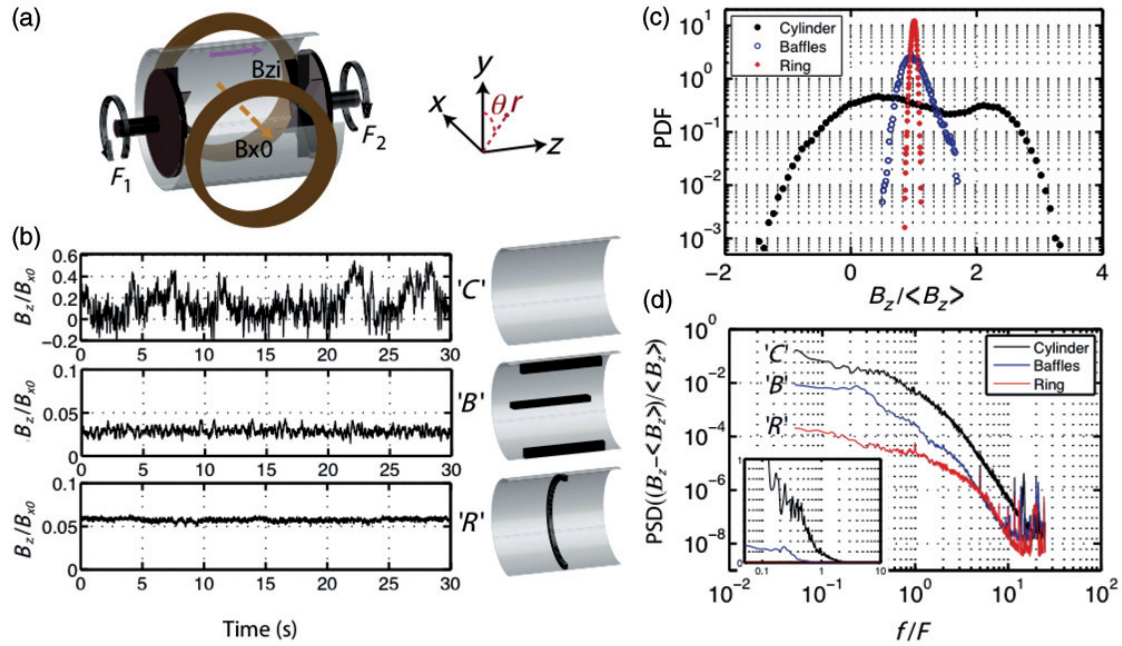
Figure 6. Transverse induction: (a) experimental set-up, (b) temporal evolution of axial induction $B_z^I(t)$ for a constant transverse applied field B_x^A, (note the difference in y-axis scales), (c) PDF and (d) time spectra of normalized induced fields – log–lin representation in the inset.

3.2.1. Turbulent BC induction. Induction measurements are performed with a constant field, applied perpendicularly to the cylinder axis. The induced field in the axial direction is measured in the mid-plane at 90° from the applied field, at distance $0.87R$ from the axis.

- C configuration. The induced field (figure 6(b)) shows a highly fluctuating dynamics. As seen in figure 6(c), the induced field distribution is bimodal, with a peak near zero induction and one at about twice the time-averaged value. The induction follows the dynamics of the radial vortices formed in the shear layer. A significant induced field is measured only when radial vortices sweep the probe. In between these events, the induced field is weak with large fluctuations – the sign of the induced field is not prescribed.
- B configuration. As compared to the above situation, the induced field is always non-zero, a feature consistent with the observation (Ravelet 2005) that the radial vortices are now confined between the baffles. A concurrent feature is that the fluctuations of induction are much reduced (a factor of 5 lower than the C configuration). The spectra displayed in figure 6 show that this reduction occurs at all scales.
- R configuration. The induction signal is again stationary and lot less fluctuating. This is consistent with observations (Ravelet 2005, Cortet *et al.* 2009) that the radial vortices within the shear layer are attached to the central ring and their strengths and low-frequency fluctuations are drastically reduced. The fluctuations are reduced again by a factor of 5 (as also seen in figure 6(c)) and this reduction lies essentially in the low-frequency motions (figure 6(d)), as measured in water for the velocity fluctuations.
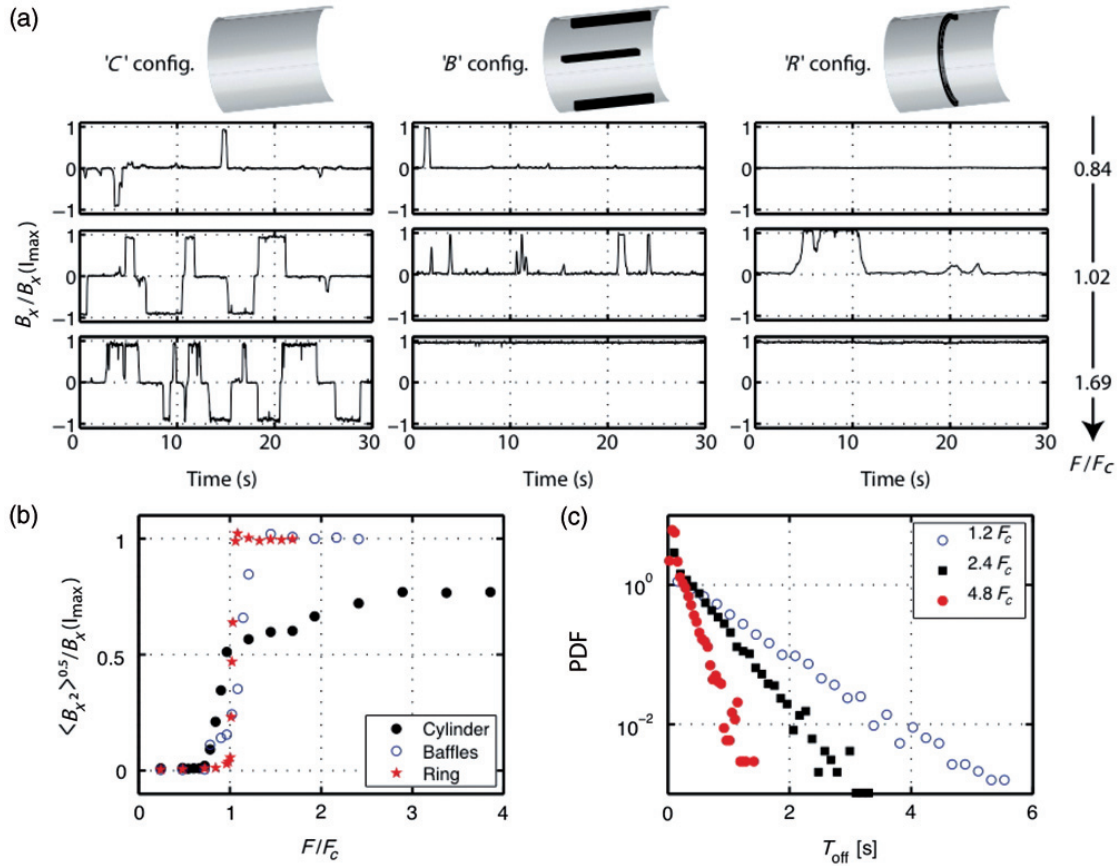
Figure 7. Equatorial dipole dynamo behavior: (a) time signals for increasing values of the rotation rate of the impellers, from below to above threshold, (b) bifurcation curves, and (c) PDF of the "off" phases for the *C* configuration, i.e., the reversing dynamo.

For the three configurations, mean induced field and normalized fluctuations at $R_m = 2$ are the following: $\langle B_z^I / B_x^A \rangle = 0.029; 0.029; 0.058$ and $(B_z^I)_{\rm rms}/\langle B_z^I \rangle = 0.90; 0.17; 0.03$ for the *C*, *B*, and *R* configurations, respectively.

3.2.2. Dynamo: equatorial dipole.   Time recordings of the equatorial dipole dynamo field are shown in figure 7(a). In each configuration, time signals are shown for three values of the rotation rates of the impeller, from below the critical frequency to above.

When compared to the previous axial dynamo cases, several features emerge. First, in the absence of appendices in the vessel (configuration *C*), a dynamo field grows with either polarity and reverses spontaneously. Below threshold, bursts with both polarities $\pm\mathbf{B}_{\rm eq}$ are observed. For higher values of the rotation rate, the fraction of time spent in a dynamo state increases. This is in sharp contrast with the *B* and *R* configurations for which homopolar dynamos are always generated after a rather abrupt bifurcation. In these configurations, bursts of dynamo action are observed near threshold, but a steady state with a definite polarity is rapidly reached above threshold.

Let us describe and analyze in detail the *C* configuration for which the magnetic field exhibits reversals. The bifurcation curve, displayed in figure 7(b)-black shows a smooth transition from the null field regime to the dynamo regime. This transition occurs

through bursts of both polarities below and around threshold. The time spent in the dynamo regime increases with the forcing parameter. As compared to all other Bullard–von Kármán dynamos obtained so far, a striking feature is that the reversing dynamo displays significant "off" phases even well above threshold. The PDFs of the "off" phases for three values of the forcing parameter are shown in figure 7(c). The observed statistic is consistent with a Poisson distribution having a characteristic time scaling as $(F/F_c)^{-1}$. On the other hand, the distributions of the duration of the saturated ("on"; plus or minus) states (not shown) are consistent with a sum of two Poisson distributions with characteristic times in a ratio of 7 and scaling as F/F_c. Note that in this configuration, statistics are converged only when working with very large time recordings. Regimes at large F/F_c have thus been obtained by increasing the gain G in order to keep F in the optimal range for operation with the liquid gallium kept at constant temperature (around 40°C).

For the B and R configurations, the dynamics of the homopolar dynamo is very similar to the previous axial case. The on–off intermittent behavior is controlled by the low-frequency content of the induction process: it is here restricted to a very narrow range of F around F_c.

As a partial conclusion here, the equatorial dynamo also develops via an on–off intermittent regime, but some features have been significantly changed, such as the ability of the dynamo to undergo reversals of polarity. These reversals are only observed when strong fluctuations are present. This is a common feature of reversals dynamics when caused by stochastic transitions between the symmetric $\mathbf{B}$ and $-\mathbf{B}$ states (Benzi and Pinton *et al.* 2009).

3.3. *Global rotation*

In this section, we address the case where the flow is driven with impellers counter-rotating at different rotations rates in the presence of a ring. This is an asymmetric R configuration, as for the dynamical regimes of the VKS dynamo reported in Berhanu *et al.* (2007), Monchaux *et al.* (2008) and Aumaître *et al.* (2009). In order to emphasize the influence of the dynamics of the mid-plane shear layer and its links with reversals, we focus on the equatorial dynamo loop.

3.3.1. *BC induction with asymmetric forcing.*
As $\Theta = (F_1 - F_2)/(F_1 + F_2)$ is varied, one observes a clear transition in the torques Γ_i driving the two impellers. Figure 8(b) shows the dimensionless differences between the torques of the two impellers (these torques are deduced from the currents measured by the electrical drives that feed the motors). The bifurcation between a 2-cell flow and a 1-cell flow occurs at a critical value $\Theta^c \sim 0.16$, in agreement with measurements made in water flows (Ravelet *et al.* 2004, Cortet *et al.* 2009).† For $|\Theta| < \Theta^c$ the time-averaged flow consists of two main cells on either side of the mid-plane, in which the toroidal and poloidal flows have opposite directions. Note that the regimes previously described correspond to a symmetric forcing, i.e., $\Theta = 0$. For $|\Theta| > \Theta^c$ the flow volume is dominated by one cell driven by the fast impeller, as is

---

†The impellers used to drive the water experiment in Ravelet *et al.* (2004) and Cortet *et al.* (2009) were of a different geometry than in this present study. Their disks were fitted with curved blades, while straight blades are used here.
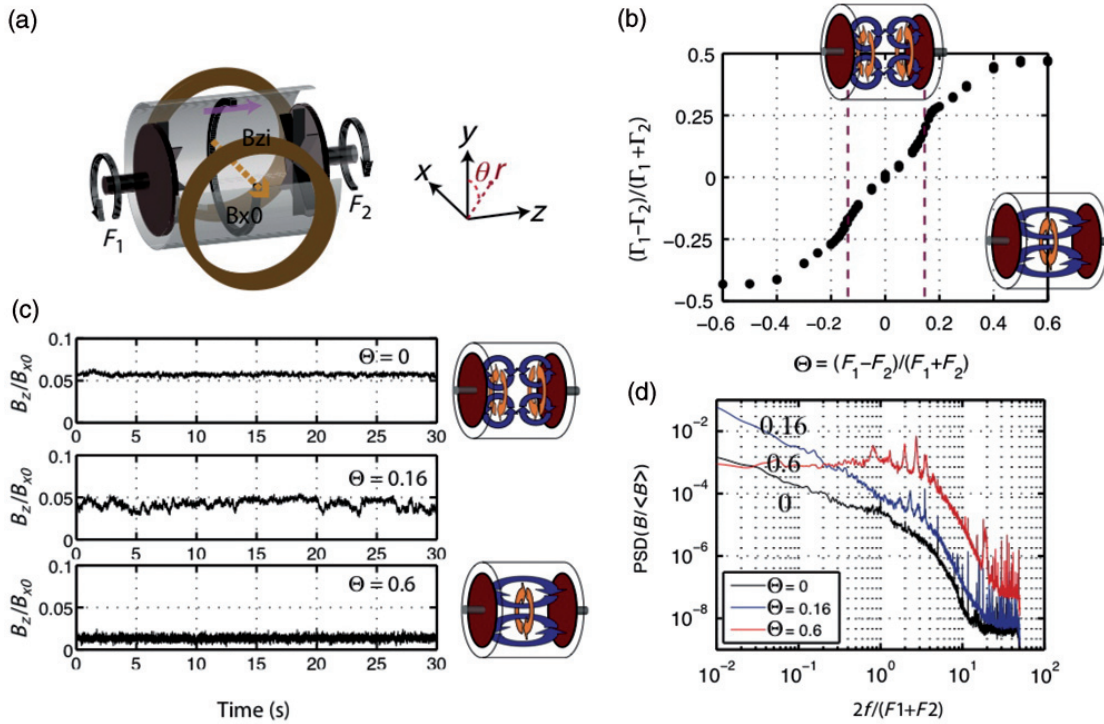
Figure 8. Influence of global rotation on *BC* induction features: (a) time signals for three values of the global rotation, (b) dimensionless torque difference as the function of the flow asymmetry – insets show sketches of the mean von Kármán flows, (c) time evolution of the induced field, and (d) corresponding power spectra.

schematically drawn in figure 8(b). It was shown in previous studies in water flows (Cortet *et al.* 2009) that fluctuations of the flow kinetic energy diverge at the transition between the two flow regimes.

Figure 8(a) shows that fluctuations of magnetic induction strongly depend on the asymmetry of the forcing. Energy distribution across scales of the turbulent-induced field also strongly depend on the asymmetry of the forcing as can be seen in figure 8(c). Near $\Theta \sim 0.16$ (shear layer instability) the low-frequency part of the spectrum is enhanced. At higher Θ values, the spectrum is enhanced around and above the forcing frequency. One thus estimates that the flow has slow large scales fluctuations only near Θ^c, while it has larger small scale fluctuations for $\Theta \gg \Theta^c$.

Evolutions of the mean-induced field and normalized fluctuations at $R_m = 2$ as a function of global rotation are the following: $\langle B_z^I / B_x^A \rangle = 0.058; 0.040; 0.013$ and $(B_z^I)_{\text{rms}} / \langle B_z^I \rangle = 0.03; 0.16; 0.22$ for the $\Theta = 0; 0.16; 0.6$, respectively.

3.3.2. Asymmetric equatorial dynamo. Time evolution of the equatorial dynamo field B_x is shown in figure 9 for three values of Θ (refer to figure 7 for the $\Theta = 0$ case) and increasing values of the rotation rate F.

The $\Theta = 0$ case, described in section 3.2, showed an homopolar dynamo with an on–off intermittent regime at onset and a steep transition from the null-field regime to the dynamo regime. When increasing Θ, a first observation is that both polarities occur, with chaotic reversals for $\Theta \sim \Theta^c$. This feature disappears for higher values of Θ, i.e., when the flow has bifurcated toward the one-cell configuration, and one recovers an
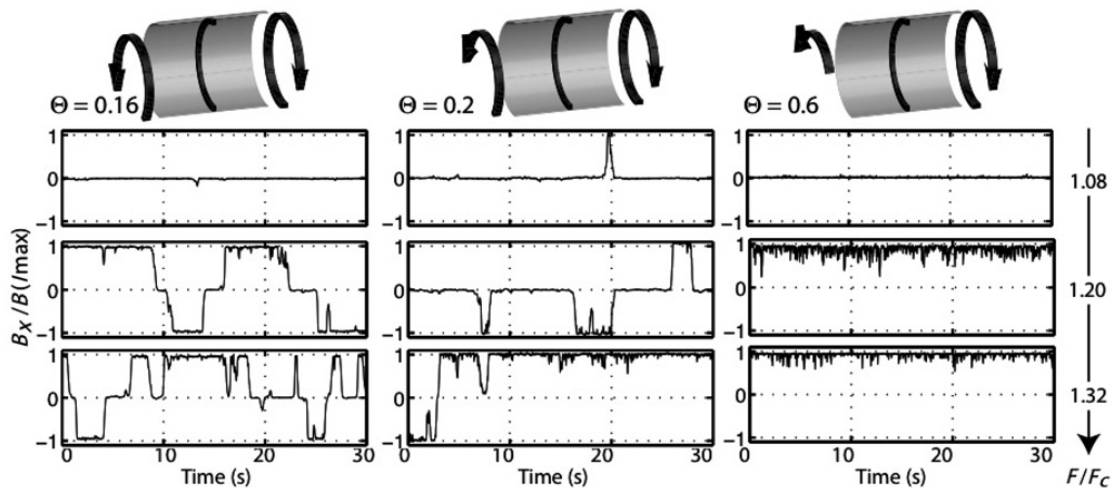
Figure 9. Transverse dynamo with global rotation: time recordings of the transverse magnetic field, for increasing values of Θ (left to right) and for increasing value of the mean rotation rate F.

homopolar dynamo. The analysis of the $\Theta \sim \Theta^c$ regimes is of great interest since, for these regimes, the VKS dynamo displayed most of its dynamical regimes (chaotic reversals, symmetric and asymmetric bursts, oscillations, etc.) (Berhanu *et al*. 2007, Monchaux *et al*. 2008, Aumaître *et al*. 2009). At the critical value $\Theta \sim \Theta^c$, the equatorial dynamo is bipolar, bifurcates through an on–off scenario and reverses chaotically. Close to the threshold value (the $\Theta = 0.2$ regime is displayed in figure 9), the dynamo also bifurcates via an on–off scenario and exhibits bursts of both polarities for a rotation rate close to F_c. At higher rotation rates, reversals occurrences are less frequent and the dynamo eventually reaches an homopolar regime for $F/F_c > 1.5$.

When the flow has bifurcated to the one-cell configuration, the equatorial dynamo is homopolar. On/off intermittency is observed in a very narrow range of driving frequencies.

4. Concluding remarks

In the present study, influence of the flow fluctuations on synthetic Bullard–von Kármán dynamos has been investigated. Two types of dynamo loops were studied: an $A - \omega$ and a $A - BC$ dynamo, where the ω and BC-effects incorporate turbulent fluctuations. Flow fluctuations modifications have been achieved by inserting appendices in the vessel, or by driving the flow asymmetrically (for $A - BC$ dynamo). Several robust features have been observed:

- The bifurcation occurs via an on–off intermittent regime at onset of dynamo action.
- The on–off intermittent regime is controlled by the low frequency part of the fluctuating induction process considered in the dynamo loop: the higher the low frequencies of the fluctuations, the wider is the occurrence of on–off intermittency among the control parameter.

- For all studied configurations, the system spends half ot its time in the dynamo regime when driven at the critical forcing parameter defined on time-averaged induction processes.

However, some features strongly depend on the exact configuration. Reversing dynamos have been observed only for strong fluctuations of the turbulent induction process. The low frequency part of the spectrum seems to play also a dominant role on the ability of the dynamo to reverse.

Hence, for this synthetic dynamo, salient features such as bursts of magnetic field activity or reversals are controlled by the underlying hydrodynamics. A detailed comparison with the dynamics of stochastic differential equations in the presence of noise is underway and will be reported elsewhere.

Acknowledgements

References

Alexakis, A. and Ponty, Y., Effect of the Lorentz force on on–off dynamo intermittency. *Phys. Rev. E* 2008, **77**, 056308.

Aumaître, S., Berhanu, M., Bourgoin, M., Chiffaudel, A., Daviaud, F., Dubrulle, B., Fauve, S., Marié, L., Monchaux, R., Mordant, N., Odier, Ph., Pétrélis, F., Pinton, J.-F., Plihon, N., Ravelet, F. and Volk, R., The VKS experiment: turbulent dynamical dynamos. *C. R. Phys.* 2008, **9**, 689–701.

Aumaître, S., Berhanu, M., Bourgoin, M., Chiffaudel, A., Daviaud, F., Dubrulle, B., Fauve, S., Marié, L., Monchaux, R., Mordant, N., Odier, Ph., Pétrélis, F., Pinton, J.-F., Plihon, N., Ravelet, F. and Volk, R., The VKS experiment: turbulent dynamical dynamos. *Phys. Fluids* 2009, **21**, 035108.

Aumaître, S., Mallick, K. and Pétrélis, F., Effects of the low frequencies of noise on on–off intermittency. *J. Stat. Phys.* 2006, **123**, 909–927.

Aumaître, S., Pétrélis, F. and Mallick, K., Low-frequency noise controls on–off intermittency of bifurcating systems. *Phys. Rev. Lett.* 2005, **95**, 064101.

Benzi, R. and Pinton, J.-F. Magnetic reversals in a simple model of MHD, submitted, arXiv, http://arxiv.org/abs/0906.0427, June 2009.

Berhanu, M., Monchaux, R., Bourgoin, M., Moulin, M., Odier, Ph., Pinton, J.-F., Volk, R., Fauve, S., Mordant, N., Pétrélis, F., Chiffaudel, A., Daviaud, F., Dubrulle, B., Gasquet, C., Marié, L. and Ravelet, F., Magnetic field reversals in an experimental turbulent dynamo. *Europhys. Lett.* 2007, **77**, 59007.

Berhanu, M., Gallet, B., Monchaux, R., Bourgoin, M., Odier, Ph., Pinton, J.-F., Plihon, N., Volk, R., Fauve, S., Mordant, N., Pétrélis, F., Aumaître, S., Chiffaudel, A., Daviaud, F., Dubrulle, B. and Ravelet, F., Bistability between a stationary and an oscillatory dynamo in a turbulent flow of liquid sodium, submitted to. *J. Fluid Mech.* 2009, **641**, 217–226.

Berthet, R., Petrossian, A., Residori, S., Romand, B. and Fauve, S., Effect of multiplicative noise on parametric instabilities. *Physica D* 2003, **174**, 84–99.

Bourgoin, M., Volk, R., Frick, P., Kripechenko, S., Odier, P. and Pinton, J.-F., Induction mechanisms in von Kármán swirling flows of liquid gallium. *Magnetohydrodynamics* 2004a, **40**, 13–31.

Bourgoin, M., Odier, P., Pinton, J.-F. and Ricard, Y., An iterative study of time independent induction effects in magnetohydrodynamics. *Phys. Fluids* 2004b, **16**, 2529–2547.

Bourgoin, M., Volk, R., Plihon, N., Augier, P., Odier, P. and Pinton, J.-F., A Bullard–von Kármán dynamo. *New J. Phys.* 2006, **8**, 329.

Brandenburg, A. and Subramanian, K., Astrophysical magnetic fields and nonlinear dynamo theory. *Phys. Rep.* 2005, **417**, 1–209.

Bullard, E.C., The stability of a homopolar dynamo. *Proc. Camb. Phil. Soc.* 1955, **51**, 744.

Cortet, P.P., Diribarne, P., Monchaux, R., Chiffaudel, A., Daviaud, F. and Dubrulle, B., Normalized kinetic energy as a hydrodynamical global quantity for inhomogeneous anisotropic turbulence. *Phys. Fluids* 2009, **21**, 025104.

Covas, E., Tavakol, R., Ashwin, P., Tworkowski, A. and Brooke, J.M., In–out intermittency in partial differential equation and ordinary differential equation models. *Chaos* 2001, **11**, 404–409.

de la Torre, A. and Burguete, J., Slow dynamics in a turbulent von Karman swirling flow. *Phys. Rev. Lett.* 2007, **99**, 054101.

Denisov, S., Noskov, V., Stepanov, R. and Frick, P., Measurements of turbulent magnetic diffusivity in a liquid-gallium flow. *JETP Lett.* 2008, **88**, 167–171.

Feng, D.L., Yu, C.X., Xie, J.L. and Ding, W.X., On–off intermittencies in gas discharge plasma. *Phys. Rev. E* 1998, **58**, 3678–3685.

Hammer, P.W, Platt, N., Hammel, S.M., Heagy, J.F. and Lee, B.D, Experimental observation of on–off intermittency. *Phys. Rev. Lett* 1994, **73**, 1095–1098.

Heagy, J.F, Platt, N. and Hammel, S.M., Characterization of on–off intermittency. *Phys. Rev. E* 1994, **49**, 1140–1150.

John, T., Stannarius, R. and Behn, U., On–off intermittency in stochastically driven electrohydrodynamic convection in nematics. *Phys. Rev. Lett.* 1999, **83**, 749–752.

Krause, F. and Rädler, K.-H., *Mean-Field Magnetohydrodynamics and Dynamo Theory*, 1980 (Oxford: Pergamon).

Laguerre, R., Nore, C., Ribeiro, A., Léorat, J., Guermond, J.-L. and Plunian, F., Impact of turbines in the VKS2 dynamo experiment. *Phys. Rev. Lett.* 2008, **101**, 104501.

Moffatt, H.K., *Magnetic Field Generation in Electrically Conducting Fluids*, 1978 (Cambridge: Cambridge University Press).

Monchaux, R., Berhanu, M., Aumaître, S., Chiffaudel, A., Daviaud, F., Dubrulle, B., Ravelet, F., Bourgoin, M., Odier, Ph., Pinton, J.-F., Plihon, N., Volk, R., Fauve, S., Mordant, N. and Pétrélis, F., Chaotic dynamos generated by a turbulent flow of liquid sodium. *Phys. Rev. Lett.* 2008, **101**, 074502.

Monchaux, R., Berhanu, M., Bourgoin, M., Moulin, M., Odier, Ph., Pinton, J.-F., Volk, R., Fauve, S., Mordant, N., Pétrélis, F., Chiffaudel, A., Daviaud, F., Dubrulle, B., Gasquet, C., Marié, L. and Ravelet, F., Generation of magnetic field by dynamo action in a turbulent flow of liquid sodium. *Phys. Rev. Lett.* 2007, **98**, 044502.

Noskov, V., Stepanov, R., Denisov, S., Frick, P., Verhille, G., Plihon, N. and Pinton, J.-F., Dynamics of a turbulent spin-down flow inside a torus. *Phys. Fluids* 2009, **21**, 045108.

Odier, P., Pinton, J.-F. and Fauve, S., Advection of a magnetic field by a turbulent swirling flow. *Phys. Rev. E* 1998, **58**, 7397–7401.

Pétrélis, F., Bourgoin, M., Marié, L., Chiffaudel, A., Fauve, S., Daviaud, F., Odier, P. and Pinton, J.-F., Non linear induction in a swirling flow of liquid sodium. *Phys. Rev. Lett.* 2003, **90**(17), 174501.

Pétrélis, F., Mordant, N. and Fauve, S., On the magnetic fields generated by experimental dynamos. *Geophys. Astro Fluid.* 2007, **101**, 289–323.

Rädler, K.H. and Stepanov, R., Mean electromotive force due to turbulence of a conducting fluid in the presence of mean flow. *Phys. Rev. E* 2006, **73**, 056311.

Ravelet, F., Bifurcations globales hydrodynamiques et magnétohydrodynamiques dans un écoulement de von Kármán turbulent, Ph.D. thesis, Ecole Polytechnique, 2005.

Ravelet, F., Chiffaudel, A. and Daviaud, F., Supercritical transition to turbulence in an inertially driven von Kármán closed flow. *J. Fluid Mech.* 2008, **601**, 339–364.

Ravelet, F., Marie, L., Chiffaudel, A. and Daviaud, F., Multistability and memory effect in a highly turbulent flow: experimental evidence for a global bifurcation. *Phys. Rev. Lett.* 2004, **93**, 164501.

Stepanov, R., Volk, R., Denisov, S., Frick, P., Noskov, V. and Pinton, J.-F., Induction, helicity and alpha effect in a toroidal screw flow of liquid gallium. *Phys. Rev. E* 2006, **73**, 046310.

Sweet, D., Ott, E., Antonsen, T.M., Lathrop, D.P. and Finn, J.M., Blowout bifurcations and the onset of magnetic dynamo action. *Phys. Plasmas* 2001, **8**, 1944–1952.

Volk, R., Odier, P. and Pinton, J.-F., Fluctuation of magnetic induction in von Kármán swirling flows. *Phys. Fluids* 2006, **18**, 085105.